

Differentiable Room Acoustic Rendering with Multi-View Vision Priors (Supplementary Material)

Anonymous ICCV submission

Paper ID 4

001 **Contents**

002 **1. Method Details** 1

003 1.1. Acoustic Beam Tracing Algorithm 1

004 1.2. Local Variance Derivation 1

005 1.3. Basis Points Sampling 2

006 1.4. Hyperparameters 2

007 1.5. Optimization 2

008 **2. Additional Results on RAF [1] Dataset and**

009 **HAA [13] Dataset** 2

010 2.1. Wave Comparison 2

011 2.2. Multi-scale Performance Comparison 4

012 2.3. Full Metric on HAA Dataset 4

013 2.4. Ablations on Vision Features 4

014 **1. Method Details**

015 **1.1. Acoustic Beam Tracing Algorithm**

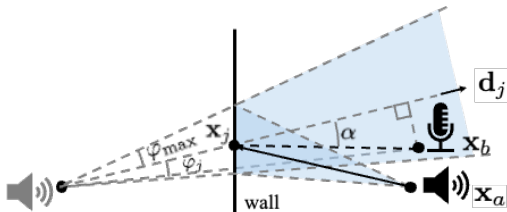


Figure 1. Acoustic beam tracing: in acoustic beam tracing the source and listener are considered as two point, the sound is propagate via a cone-shape beam in space. Acoustic beam tracing handles reflection the same as ray tracing does. The key difference is that acoustic beam tracing enumerate a reflection path if the listener is contained in the beam volume but not necessarily being hit by the sampled ray

016 Given the source location \mathbf{x}_a and listener location \mathbf{x}_b , we
 017 adopt acoustic beam tracing [2, 4, 7, 12] to sample specular
 018 beams in a source-to-listener manner. First we cast N_d
 019 beams from the source, using a Fibonacci lattice [3] to ap-
 020 proximate uniform coverage of directions. A small apex

angle $2\varphi_{\max}$ is selected to ensure the cone-shape beams re-
 main disjoint. Next, each beam’s center ray intersects with
 room geometry to find reflection points (e.g. via Open3D
 [14]), and after each reflection, we check if the reflected
 beam can hit the listener. To determine whether a reflected
 beam at j -th reflection point \mathbf{x}_j (with out-going direction
 \mathbf{d}_j) reaches the listener before hitting another surface, we
 check if the listener is within the reflected cone (as show in
 Figure 1). Denote l_j as the distance traveled by reaching
 \mathbf{x}_j , and α_j as the angle between \mathbf{d}_j and the line from \mathbf{x}_j to
 \mathbf{x}_b and φ_j as the sampled half-apex angle:

$$\varphi_j = \arctan \left(\frac{\|\mathbf{x}_b - \mathbf{x}_j\| \sin \alpha}{\|\mathbf{x}_b - \mathbf{x}_j\| \cos \alpha + l_j} \right). \quad (1)$$

The listener is considered “hit” if α is acute, $\varphi_j < \varphi_{\max}$,
 and \mathbf{x}_j is visible by \mathbf{x}_b . In addition, the time-of-arrival is
 by:

$$t_{\text{oa}_j} = \frac{\|\mathbf{x}_b - \mathbf{x}_j\| \sin \alpha}{v_{\text{sound}} \cdot \sin \varphi_j}. \quad (2)$$

Algorithm 1 summarizes our beam-tracing procedure.

1.2. Local Variance Derivation

As shown in Figure 2, consider a beam traveling distance
 l before hitting the surface at \mathbf{x} , with half-apex angle φ
 and local surface normal \mathbf{z} . Let θ be the angle between
 the reflected direction \mathbf{d} and \mathbf{z} . In a local coordinate system
 whose axes are $\{\mathbf{t}_1, \mathbf{t}_2, \mathbf{z}\}$, where we requires \mathbf{t}_1 aligns with
 the projection of \mathbf{d} in the tangent surface, the beam’s cross-
 section at distance l is approximately an ellipse with semi-
 major and semi-minor axes proportional to $l \sin \varphi$, modu-
 lated by θ . A simple way to encode this elliptical patch is to
 use a diagonal covariance at local coordinate

$$\Sigma_{\text{local}} = \text{diag}(\sigma_1^2, \sigma_2^2, 0), \quad (3)$$

where σ_1^2 and σ_2^2 grow with $l \sin \varphi$, adjusted by $\cos \theta$. In the
 case when φ is small:

$$\sigma_1^2 \approx (l \sin \varphi)^2 / \cos^2 \theta, \quad \sigma_2^2 \approx (l \sin \varphi)^2 / \cos \theta. \quad (4)$$

Algorithm 1: Acoustic Beam Tracing

```

Input: Source  $\mathbf{x}_a$ , Listener  $\mathbf{x}_b$ , Geometry  $\mathcal{M}$ 
Output: Specular paths  $\{\tilde{\mathbf{x}}_k\}_{k=1}^N$ 
for  $i = 1$  to  $N_d$  do
     $\mathbf{x}_{i,0} \leftarrow \mathbf{x}_a; l_{i,0} \leftarrow 0;$ 
     $\mathbf{d}_{i,0} \leftarrow \text{SampleFib}(N_d, i)$ 
end
ANS  $\leftarrow \{\}$ 
if  $IsVisible(\mathbf{x}_a, \mathbf{x}_b)$  then
    | ANS.add( $\emptyset$ ) // direct path
end
for  $j = 1$  to  $MAX_{depth}$  do
    for  $i = 1$  to  $N_d$  do
         $[\mathbf{x}_{i,j}, \mathbf{z}] = \text{HitPoint}(\mathcal{M}, \mathbf{x}_{i,j-1}, \mathbf{d}_{i,j-1})$ 
         $\mathbf{d}_{i,j} = \mathbf{d}_{i,j-1} - 2(\mathbf{z}^\top \mathbf{d}_{i,j-1})\mathbf{z}$ 
         $l_{i,j} = l_{i,j-1} + \|\mathbf{x}_{i,j} - \mathbf{x}_{i,j-1}\|$ 
        if  $BeamHit(\mathbf{x}_b, \mathbf{x}_{i,j}, \mathbf{d}_{i,j}, l_{i,j})$  then
            | ANS.add( $[\mathbf{x}_{i,1}, \mathbf{x}_{i,2}, \dots, \mathbf{x}_{i,j}]$ )
        end
    end
end
return ANS

```

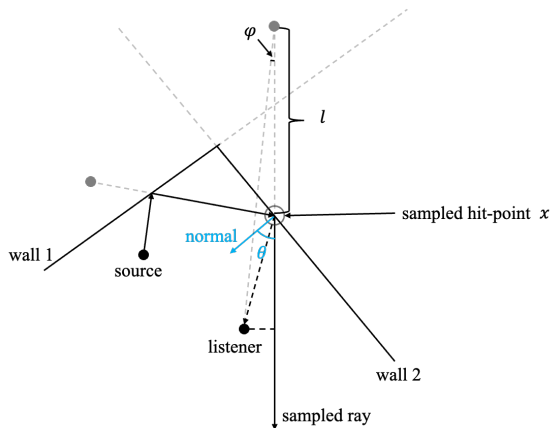


Figure 2. Local covariance derivation: as the traveling space l increases, the region of the contact area expand linearly in terms of radius. In addition, since the half-apex angle is assumed to be small, the contact region is considered an ellipse, which motivates use model the region information with a gaussian distribution.

053 These terms capture how the beam’s ellipse “stretches”
 054 along \mathbf{t}_1 and \mathbf{t}_2 . In world coordinates, the final covariance
 055 Σ is simply

056
$$\Sigma = Q \Sigma_{local} Q^\top,$$

057 where $Q = [\mathbf{t}_1 \mathbf{t}_2 \mathbf{z}]$ rotates from local axes to world axes.

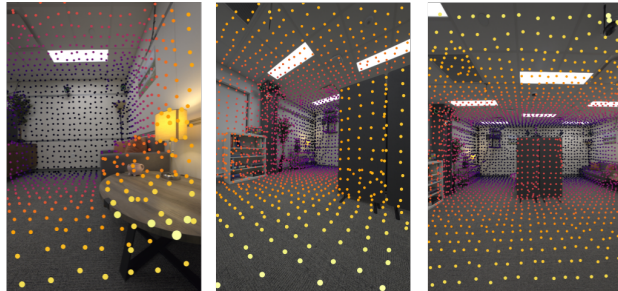


Figure 3. Visualization of surface basis samples for extracting multi-view images features.

1.3. Basis Points Sampling

we sample the basis point in two steps, first we densely sample 100,000 points on the room geometry, then, we down-sample them with voxel size 0.2m and use the median point (closest to mean point) as the basis samples for vision features, as shown in Figure 3, in this way, we ensures the distances between samples are stable.

1.4. Hyperparameters

Following [13], we use a spherical Gaussian weighting function with a sharpness parameter of 8 for source directional response. We decode the image feature using a 4-layer MLP and sample frequencies from 12 to 7800 Hz with 16 logarithmically spaced samples, linearly interpolating the frequency response.

1.5. Optimization

We optimize the network using the AdamW optimizer with a fixed learning rate of 5×10^{-4} (and 1×10^{-4} for the residual component). Our loss function is defined as:

$$\mathcal{L} = \mathcal{L}_{MAG} + \lambda_{pink} \mathcal{L}_{pink}, \tag{4}$$

where \mathcal{L}_{MAG} is a multi-scale log L1 loss, and \mathcal{L}_{pink} is the pink noise supervision loss. We adopt a progressive training strategy, starting with a reflection order $N = 1$ and increasing by 1 every 100 epochs until $N = 6$. During training, we sample 16,384 points from Fibonacci lattices for beam tracing, reducing this to 8,192 points per RIR during inference. Training is performed with a batch size of 1.

2. Additional Results on RAF [1] Dataset and HAA [13] Dataset

2.1. Wave Comparison

Figure 4 shows wave visualizations on the Hearing Anything Anywhere dataset. All models were trained on only 12 data points. Our model significantly outperforms the baselines in preserving the wave structure, producing a wave front that closely matches the ground truth in terms of peak

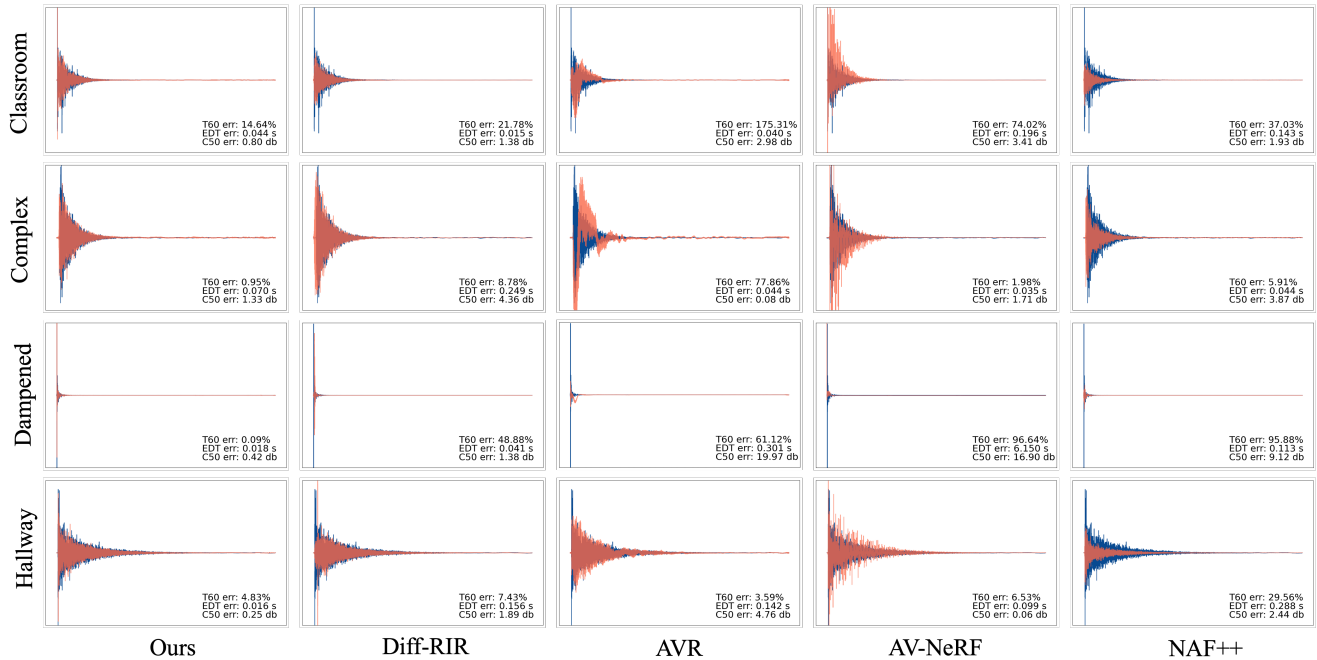


Figure 4. Wave visualization on the Hearing Anything Anywhere dataset [13]. All models are trained on 12 data points. Our model significantly outperforms all baselines in preserving the wave structure—producing the most faithful wave front with accurate peak locations and magnitudes. Note that quantitative metrics do not always capture these perceptual details; some methods may have low error values despite producing distorted wave patterns.

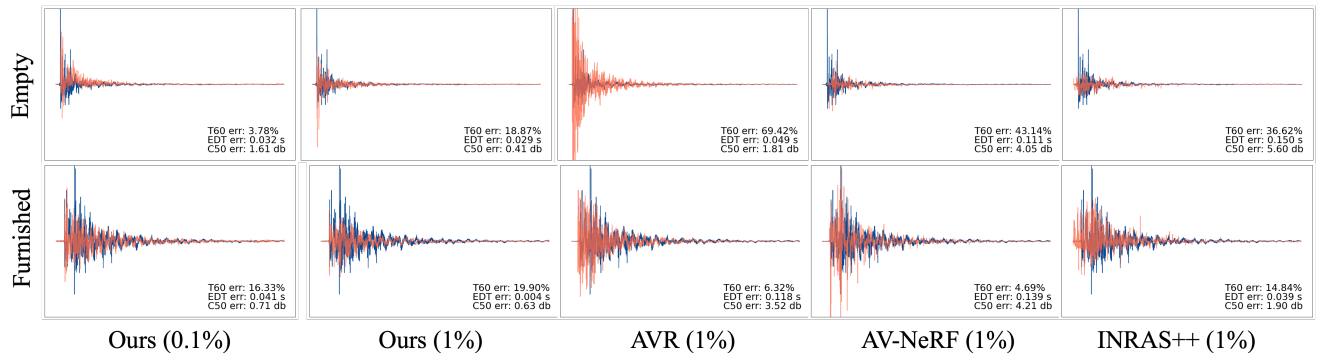


Figure 5. Wave visualization on the Real Acoustic Field dataset [1]. We show results from three baseline models trained on 1% of the data alongside our model trained on 1% and 0.1% of the data. Our model exhibits better peak alignment and magnitude than baseline methods—even when trained on only 0.1% of the data—and significantly outperforms all baselines when using the same amount of training data.

092 locations and magnitudes. Note that quantitative metrics
 093 do not always capture these perceptual differences; some
 094 methods may achieve low error values despite generating
 095 distorted wave patterns. This comparison highlights the su-
 096 perior capability of our approach in modeling acoustic dy-
 097 namics in few-shot settings.

098 Figure 5 presents wave visualizations on the Real Acous-
 099 tic Field dataset. Here, we compare three baseline models
 100 trained on 1% of the data with our model trained on both 1%

and 0.1% of the data. Our results demonstrate that, in terms
 of wave structure, our model achieves better peak align-
 ment and peak magnitude than the baselines—even when
 our model is trained on only 0.1% of the data. When trained
 on 1% of the data, our method further outperforms the base-
 lines.

101
 102
 103
 104
 105
 106

107 **2.2. Multi-scale Performance Comparison**

108 Figure 6 extend the multi-scale performance comparison in
 109 main paper by evaluating on two more metrics, i.e., Loud-
 110 ness and EDT. The result shows that our model performs
 111 consistently better than baselines in all training data scale,
 which is aligned with our observation in the main paper.

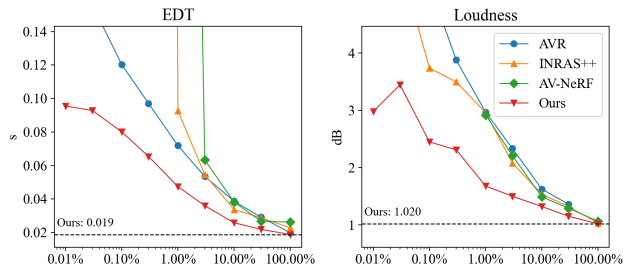


Figure 6. Performance comparison across training scales (from 0.01% to 100% of training data). In addition to the metrics reported in the main paper, our model consistently outperforms the baselines in terms of both EDT and Loudness.

112

113 **2.3. Full Metric on HAA Dataset**

114 Tables 2 and 3 present the complete evaluation metrics on
 115 the HAA dataset, including Loudness, C50, EDT, and T60
 116 across four scenes. Our results show that our method out-
 117 performs state-of-the-art baselines across almost all met-
 118 rics, confirming the trends observed in the main paper. The
 119 only exception is the C50 metric and EDT metric in the
 120 *Hallway* scene, where AV-NeRF performs particularly well,
 121 likely due to its effective use of depth information in this
 122 constrained geometry. These comprehensive results vali-
 123 date the robustness and effectiveness of our model in diverse
 124 real-world acoustic environments.

125 **2.4. Ablations on Vision Features**

126 We investigate the impact of vision features by varying two
 127 aspects: the number of multi-view images used for training
 128 and the choice of the pretrained encoder. Both experiments
 129 are conducted on the RAF Furnished scene using only 0.1%
 130 of the training data.

131 In our vision feature saturation experiment, we initially
 132 use 65 images to cover the entire scene, then reduce the
 133 number to 20, 10, and 5 views (see top four rows of Ta-
 134 ble 1). Reducing from 65 to 20 views incurs less than a
 135 1% drop in C50 and EDT, but further reduction from 20
 136 to 10 views causes a marked performance decline, indicat-
 137 ing that adequate view redundancy is essential for effective
 138 visual guidance. Performance remains stable when further
 139 reduced from 10 to 5 views, suggesting that with only 10
 140 views the model nearly abandons visual feature learning and
 141 relies primarily on acoustic cues.

We also replace the DINO-v2 [10] encoder with
 ResNet18 [5], which results in a noticeable drop in EDT,
 demonstrating that DINO-V2 is better suited for our model.
 Notably, all vision ablations have minimal impact on T60,
 indicating that vision features primarily contribute to mod-
 eling early reflection phenomena rather than late reverbera-
 tion.

142
143
144
145
146
147
148

Variant	C50	EDT	T60
65 views	1.98	80.1	15.2
20 views	2.01	80.9	15.7
10 views	2.13	97.9	15.2
5 views	2.12	97.2	15.3
ResNet18	1.96	89.4	15.3

Table 1. Ablation study on vision features. “65 views” denotes using 65 images for training; “20 views”, “10 views”, and “5 views” denote reduced image sets. “ResNet18” indicates replacing the DINO-V2 encoder with ResNet18.

Method	Classroom				Complex Room			
	Loudness (dB) ↓	C50 (dB) ↓	EDT (ms) ↓	T60 (%) ↓	Loudness (dB) ↓	C50 (dB) ↓	EDT (ms) ↓	T60 (%) ↓
NAF++ [9]	8.27	1.62	162.3	134.0	4.43	2.25	203.5	44.8
INRAS++ [11]	1.31	1.86	110.0	60.9	1.65	2.26	150.7	29.5
AV-NeRF [8]	1.51	1.43	77.8	50.0	2.01	1.88	107.9	36.6
AVR [6]	3.26	4.18	135.6	44.3	6.47	2.55	138.3	36.7
Diff-RIR [13]	2.24	2.42	139.7	39.7	1.75	2.23	129.5	18.5
Ours	0.99	1.02	55.5	24.3	0.98	1.44	86.5	10.8

Table 2. Result on Diff-RIR [13] dataset, 2.0s, 16K sample rate

Method	Dampened Room				Hallway			
	Loudness (dB) ↓	C50 (dB) ↓	EDT (ms) ↓	T60 (%) ↓	Loudness (dB) ↓	C50 (dB) ↓	EDT (ms) ↓	T60 (%) ↓
NAF++ [9]	3.88	4.24	360.0	306.9	8.71	1.36	148.3	21.4
INRAS++ [11]	3.45	3.28	187.1	382.9	1.55	1.87	157.9	7.4
AV-NeRF [8]	2.40	3.05	242.1	107.9	1.26	1.03	89.9	9.5
AVR [6]	6.65	11.11	305.3	81.4	2.48	2.69	195.4	7.0
Diff-RIR [13]	1.87	1.56	153.0	44.9	1.32	3.13	188.1	6.8
Ours	1.11	1.45	139.0	31.9	0.85	1.15	96.5	6.3

Table 3. Result on Diff-RIR [13] dataset, 2.0s, 16K sample rate

149
150
151
152
153
154
155
156
157
158
159
160
161
162
163
164
165
166
167
168
169
170
171
172
173
174
175
176
177
178
179
180
181
182
183
184
185
186
187
188
189
190
191
192
193
194
195
196
197
198
199
200
201
202
203
204
205
206**References**

- [1] Ziyang Chen, Israel D Gebru, Christian Richardt, Anurag Kumar, William Laney, Andrew Owens, and Alexander Richard. Real acoustic fields: An audio-visual room acoustics dataset and benchmark. In *Proceedings of the IEEE/CVF Conference on Computer Vision and Pattern Recognition*, pages 21886–21896, 2024. 1, 2, 3
- [2] Thomas Funkhouser, Ingrid Carlbom, Gary Elko, Gopal Pingali, Mohan Sondhi, and Jim West. A beam tracing approach to acoustic modeling for interactive virtual environments. In *Proceedings of the 25th Annual Conference on Computer Graphics and Interactive Techniques, SIGGRAPH '98*, page 21–32, New York, NY, USA, 1998. Association for Computing Machinery. 1
- [3] Douglas P. Hardin, Timothy Michaels, and Edward B. Saff. A comparison of popular point configurations on \mathbb{S}^2 . *Dolomites Research Notes on Approximation*, 9, 2016. 1
- [4] John Kenneth Haviland and Balakrishna D. Thanedar. Monte carlo applications to acoustical field solutions. *The Journal of the Acoustical Society of America*, 54(6):1442–1448, 12 1973. 1
- [5] Kaiming He, X. Zhang, Shaoqing Ren, and Jian Sun. Deep residual learning for image recognition. *2016 IEEE Conference on Computer Vision and Pattern Recognition (CVPR)*, pages 770–778, 2015. 4
- [6] Zitong Lan, Chenhao Zheng, Zhiwei Zheng, and Mingmin Zhao. Acoustic volume rendering for neural impulse response fields. In *The Thirty-eighth Annual Conference on Neural Information Processing Systems*, 2024. 5
- [7] Christian Lauterbach, Anish Chandak, and Dinesh Manocha. Interactive sound rendering in complex and dynamic scenes using frustum tracing. *IEEE Transactions on Visualization and Computer Graphics*, 13:1672–1679, 2007. 1
- [8] Susan Liang, Chao Huang, Yapeng Tian, Anurag Kumar, and Chenliang Xu. Av-nerf: Learning neural fields for real-world audio-visual scene synthesis. In *Conference on Neural Information Processing Systems (NeurIPS)*, 2023. 5
- [9] Andrew Luo, Yilun Du, Michael Tarr, Josh Tenenbaum, Antonio Torralba, and Chuang Gan. Learning neural acoustic fields. *Advances in Neural Information Processing Systems*, 35:3165–3177, 2022. 5
- [10] Maxime Oquab, Timothée Darcet, Theo Moutakanni, Huy V. Vo, Marc Szafraniec, Vasil Khalidov, Pierre Fernandez, Daniel Haziza, Francisco Massa, Alaaeldin El-Nouby, Russell Howes, Po-Yao Huang, Hu Xu, Vasu Sharma, Shang-Wen Li, Wojciech Galuba, Mike Rabbat, Mido Assran, Nicolas Ballas, Gabriel Synnaeve, Ishan Misra, Herve Jegou, Julien Mairal, Patrick Labatut, Armand Joulin, and Piotr Bojanowski. Dinov2: Learning robust visual features without supervision, 2023. 4
- [11] Kun Su, Mingfei Chen, and Eli Shlizerman. INRAS: Implicit neural representation for audio scenes. In Alice H. Oh, Alekh Agarwal, Danielle Belgrave, and Kyunghyun Cho, editors, *Advances in Neural Information Processing Systems*, 2022. 5
- [12] Dirk van Maercke and Jacques Martin. The prediction of echograms and impulse responses within the epidaure software. *Applied Acoustics*, 38(2):93–114, 1993. 1
- [13] Mason Wang, Ryosuke Sawata, Samuel Clarke, Ruohan Gao, Shangzhe Wu, and Jiajun Wu. Hearing anything anywhere. In *CVPR*, 2024. 1, 2, 3, 5
- [14] Qian-Yi Zhou, Jaesik Park, and Vladlen Koltun. Open3D: A modern library for 3D data processing. *arXiv:1801.09847*, 2018. 1

207
208
209
210
211
212